Under-expanded Impinging Supersonic Jet Flow

Julio Soria[1, 2,*] **and Omid Amili**[1]

[1]Laboratory for Turbulence Research in Aerospace and Combustion, Department of Mechanical and Aerospace Engineering, Monash University, Melbourne, VIC 3800 Australia
[2]Department of Aeronautical Engineering, King Abdulaziz University, Jeddah 21589, Kingdom of Saudi Arabia
[*]corresponding author: julio.soria@monash.edu

Abstract The physics of supersonic circular jets has been under investigation over the last five decades due to the many aerospace and industrial applications where these jets are found. When gas exists a circular nozzle with a pressure higher than the pressure of the surrounding environment, an under-expanded jet forms. In this case, the pressure of the jet reaches the ambient pressure through a series of shock and expansion waves. This situation becomes more complicated when the jet interacts with an impingement surface. Understanding of the impinging jet flow is important in the design and control of short vertical takeoff and landing (SVTOL) aircrafts and in rocket and missile launching systems. The flow field in supersonic impinging jets is highly unsteady and contains a feedback loop. This mechanism is initiated by coherent pressure fluctuations generated when the jet impacts on the solid surface and which travel upstream as sound waves to the nozzle lip where they force the shear layer, thus forming a forced feedback loop. This paper presents high-spatial resolution 2C-2D PIV measurements taken along the streamwise-radial direction on the centre plane of the jet. Experiments with nozzle pressure ratios ranging between 2 to 5 and stand-off distances in the range of 1 to 5 have been performed. The paper is aimed at addressing the flow structure and lower- and higher-order statistics only for the nozzle pressure ratio of 3.4 and the stand-off distance of 5.0.
Keywords: Supersonic jet, Under-expanded jet, Impinging supersonic jet, PIV

1 Introduction

The physics of supersonic jets has been under investigation over the last five decades due to their various aerospace and industrial applications. When a jet exists a nozzle with a pressure higher than the pressure of the surrounding area, an under-expanded jet forms. In this case, the pressure of the jet reaches the ambient pressure through a series of shock waves, and expansion waves. This situation becomes more complicated when the jet interacts with an impingement surface. Understanding of the impinging jet flow is important in the design and control of short vertical takeoff and landing (SVTOL) of aircrafts, rocket/missile launching systems [10, 11], and in the cold spray coating process [8, 1].

The flow field in supersonic impinging jets is highly unsteady. It contains a feedback loop that was first described by [15]. This mechanism is initiated by instabilities that develop in the shear layer originating from the nozzle lip. The instability waves grow in spatial extend and create large scale coherent structures that travel downstream. When they impact the impingement surface, coherent large pressure fluctuations are generated that travel upstream as acoustic waves. At the nozzle lip, these acoustic waves are internalised as perturbations which force the shear layer and thus complete the feedback loop.

The authors and co-workers have previously shown the cyclic nature of the impingement process and the closed loop instability mechanisms using two sets of high-spatial and high-temporal resolution Schlieren images of an impinging jet [2, 13]. Figure 1 visualizes the acoustic waves traveling towards the nozzle and the coherent structures at the shear layer. In the present study, high-spatial resolution measurements of the velocity fields of this phenomenon are reported. The important parameters that affect the flow structure and noise production are the nozzle pressure ratio (NPR), the Reynolds number, the nozzle to surface spacing (stand-off distance), the nozzle shape, and the impinging plate's size and angle.

The flow regime, instabilities, coherent structures, and the generated noise level are functions of these parameters especially of the stand-off distance and NPR. At a certain combination of these parameters, an amplification of the shear layer instabilities and evolution of coherent structures occurs, which creates the forced feedback loop. As shown by [11], for an impinging jet with a $x/D = 4.0$ and a nozzle pressure ratio of 3.7, the shear layer is dominated by helical instabilities. However, for $x/D = 4.5$ at the same NPR, the flow is dominated by strongly coherent and axisymmetric structures. [11] found that the former helical instability case

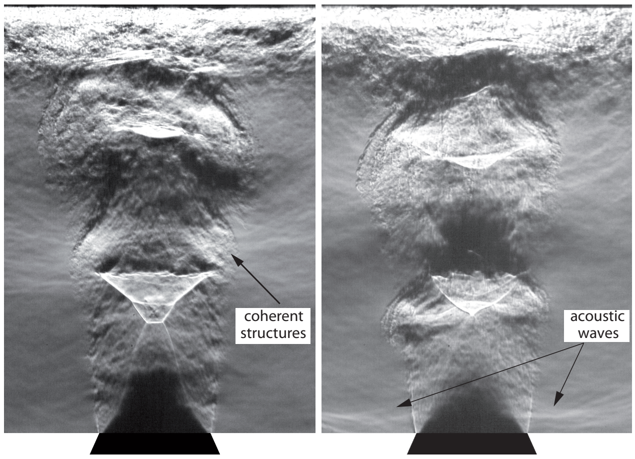

Fig. 1 Instantaneous high spatial resolution Schlieren images of $d\rho/dx$ in an under-expanded impinging circular jet flow illustrating the acoustic waves and coherent structures in a feedback loop mechanism for NPR=3.2, and x/D=4.0 [13]. Flow is from the bottom to the top.

could be controlled by micro jets, whereas the latter case containing axisymmetric structures could not, clearly showing the importance of understanding the flow instabilities that result from different operating conditions in order to control these flows.

In the present study, high spatial resolution 2C-2D PIV measurements are performed along the streamwise-radial direction contain the axis of the of the jet. Nozzle pressure ratios ranging between 2 to 5 with stand-off distances in the range of 1-5 have been investigated. The paper is aimed at addressing the flow structure and lower- and higher-order statistics only for the nozzle pressure ratio of 3.4 and the stand-off distance of 5.0.

2 Experimental Methodology

2.1 Under-expanded supersonic impinging jet flow facility

The apparatus used in this study is a re-designed and improved version of an earlier LTRAC Supersonic Jet Facility described in [14]. Compressed air at a pressure of approximately 7 bar and a temperature of approximately 20 ^{o}C is provided from the supply line into the mixing chamber of the jet facility using a high-pressure hose. The inlet compressed flow is regulated using a Fairchild high-flow pressure regulator with a pressure control range of 0-10 bar and the pressure variation of approximately 1 %. The flow temperature is monitored using thermocouples at different locations. The mixing chamber with wire mesh at both ends is connected to a plenum chamber that contains a honeycomb section followed by a number of wire meshes. This ensures that the flow is straightened and the turbulence intensity level is reduced before entering the nozzle. The stagnation pressure in the plenum chamber is measured using a RS-461 pressure transducer with an uncertainty of approximately 0.25 %.

In this experiment, a converging nozzle with the inner exit diameter of 15 mm is mounted on the top of the plenum chamber. The nozzle which was manufactured using CNC machining of a single stainless steel block has a sharp lip with a thickness of 1.5 mm. A machined insert as shown in Figure 2 is used to cover the outer region of the nozzle. A square piece of glass with a size of $15D\times15D$ is used as the impinging surface. The Reynolds number based on the fully expanded jet velocity and the nozzle exit diameter is approximately 7.1×10^5. The isentropic flow assumption is used to calculate the pressure and the temperature at the jet exit.

2.2 PIV experimental set-up and analysis

The application of particle image velocimetry (PIV) to supersonic flows is accompanied by a number of challenges as described by [18, 12]. However, once these have been adequately addressed, PIV provides reliable velocity field measurements in this type of challenging jet flow environment.

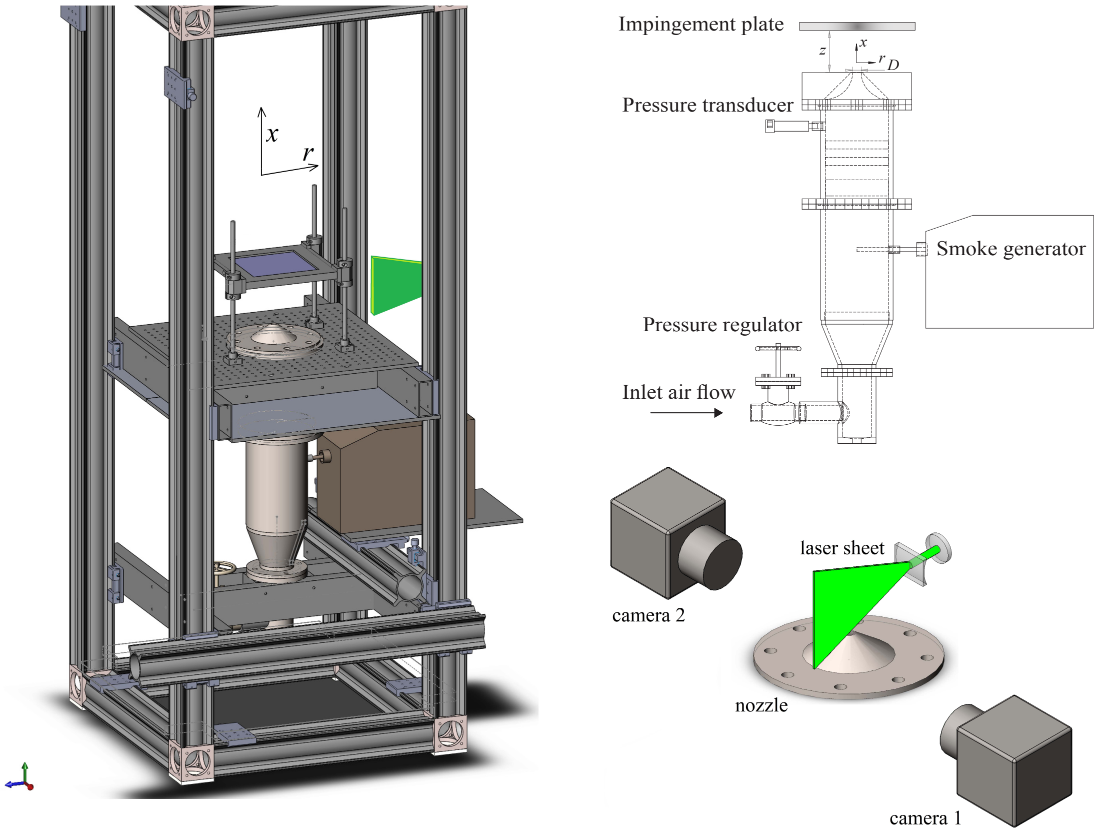

Fig. 2 A schematic diagram of the experimental facility.

A Vicount 1300 smoke generator is used to supply the seed particles by connecting it to the mixing chamber as shown in Figure 2. The smoke generator provides a persistent and high seeding density with a nominal particle size of $0.2-0.3\mu$m. In order to improve the seeding quality and decrease the possibility of oil condensation which has the potential to result in the formation of large droplets, the smoke is heated between the generator and its entry into the mixing chamber using a temperature controlled electrical heating belt. The particle relaxation time is estimated to be 2.0 μs based on the approach described in [14]. The corresponding effective particle diameter is approximately 0.6 μm.

In this study, two 12-bit Imperx B6640 camera with a CCD array of 6,600 $\times$ 4,400 px^2 and a square pixel size of 5.5μm are used as the imaging sensors. A dual-cavity Nd:YAG pulsed laser with a wavelength of 532 nm and a maximum pulse energy of 200 mJ is used as the illumination source. An appropriate combination of spherical and cylindrical lenses is used to reduce the beam diameter and to produce a collimated laser sheet with a thickness of approximately 1 mm. 200 mm Micro-Nikkor lenses are employed in these experiments with magnifications of approximately 0.48 and 0.8. Due to the small size of particles, the diffraction limited diameter ($\sim$ 11 μm) dominates the particle's geometric size. The depth of field estimation given in Table 1 is based on the diffraction limited image diameter, F-number, and the magnification [17]. 10,000 image pairs were recorded at a rate of 1.0 Hz. A reliable control system based on a BeagleBone Black (BBB) credit card computer developed at LTRAC was used to generate high precession triggering signals [6]. The laser pulse jitter was monitored using a photodiode and found to be of the order of 4 ns.

The single exposed image pairs were analysed using the multigrid cross-correlation digital PIV (MCCD-PIV) algorithm described in [24], which has its origin in an iterative and adaptive cross-correlation algorithm introduced by [19, 21, 20]. Details of the performance, precision and experimental uncertainty of the MC-CDPIV algorithm with applications to the analysis of single-exposed PIV and holographic PIV (HPIV) image pairs have been reported in [22, 5], respectively. The present single-exposed image acquisition experiments were designed for a two-pass MCCDPIV analysis with discrete IW offset used in the second pass to minimize

Table 1 PIV parameters

Parameter	Physical unit	Non-dim. unit	Physical unit	Non-dim. unit
	Camera 1		Camera 2	
Img. resolution	11.84μm/px	–	6.87μm/px	–
Diffraction limited dia.	$\sim 11\mu$m	–	$\sim 13\mu$m	–
Field of view*	78mm × 52mm	$5.2D \times 3.5D$	45mm × 30mm	$3.0D \times 2.0D$
Depth of field	$\sim 550\mu$m	$\sim 0.04D$	$\sim 550\mu$m	$\sim 0.04D$
IW_0*	128px × 64px	0.1 × 0.05	160px × 64px	0.6 × 0.03
IW_1	32px × 32px	$0.025D \times 0.025D$	32px × 32px	$0.015D \times 0.015D$
Vector spacing	16px × 16px	$0.012D \times 0.012D$	16px × 16px	$0.007D \times 0.007D$
Time delay	∼880ns	–	∼880ns	–

* along the streamwise and radial directions respectively.

the measurement uncertainty [25] . The MCCDPIV algorithm also employs the local cross-correlation function multiplication method introduced by [9] to improve the search for the location of the maximum value of the cross-correlation function. A two dimensional Gaussian function model was used to find, in a least square sense, the two-dimensional cross-correlation function peak to sub-pixel accuracy [19]. Each MCCDPIV velocity field was subsequently validated using the threshold cross-correlation peak value criterion ($\rho > 0.6$) and the dynamic mean value operator test described in [16]. The tests were applied in the specified order. A brief summary of the PIV parameters is provided in Table 1.

Following data validation, the in-plane velocity components (u, v) in the (x, r) coordinate directions respectively were computed by taking the optical magnification into account and by dividing the measured MCCDPIV displacement in each interrogation window by the time between the exposures of the image pair. The uncertainty relative to the maximum velocity in the velocity components at the 95% confidence level for these measurements is 0.03% [21]. The current version of the MCCDPIV algorithm uses MPI to implement parallelisation of the MCCDPIV analysis. The MCCDPIV analysis of the results presented in this paper was carried out using 36 CPU cores on the NCI Massive HPC.

The out-of-plane vorticity, ω_θ, was calculated from the MCCDPIV velocity field measurements using a local least-squares fit procedure to the velocity field, followed by analytic differentiation using the relationship

$$\omega_\theta = \partial v/\partial x - \partial u/\partial r. \tag{1}$$

A thirteen point, two-dimensional, local fit to the velocity field data was used [21, 23]. This calculation is an approximation that introduces a bias and a random error into the computed vorticity. These errors have been investigated and discussed in [7, 23]. For a vorticity distribution with a characteristic length scale of $0.191D$, the bias error is estimated as -0.3% and the random error is estimated as ±2.4% at the 95% confidence level, while for a vorticity distribution with a characteristic length scale of $0.048D$, the bias error is estimated as -4.9% and the random error is estimated as ±0.6% at the 95% confidence level.

3 Results

Figure 3 shows the velocity magnitude of an instantaneous field. The streamlines are shown in order to better visualize the quiescent fluid entrainment into the shear layer and the formation of the wall jet at the impingement surface. The jet exit velocity (U_e) that is approximately 315 m/s is used for the normalization of the velocity.

As can be seen, fine flow features are well resolved. Important flow features that cannot necessarily be inferred from the mean fields are highlighted in this figure. The visual inspection of instantaneous velocity fields shows the existence of stagnation/low-speed regions after the shock cells in the jet's potential core especially after the first shock. A higher spatial resolution measurement that was performed simultaneously with the

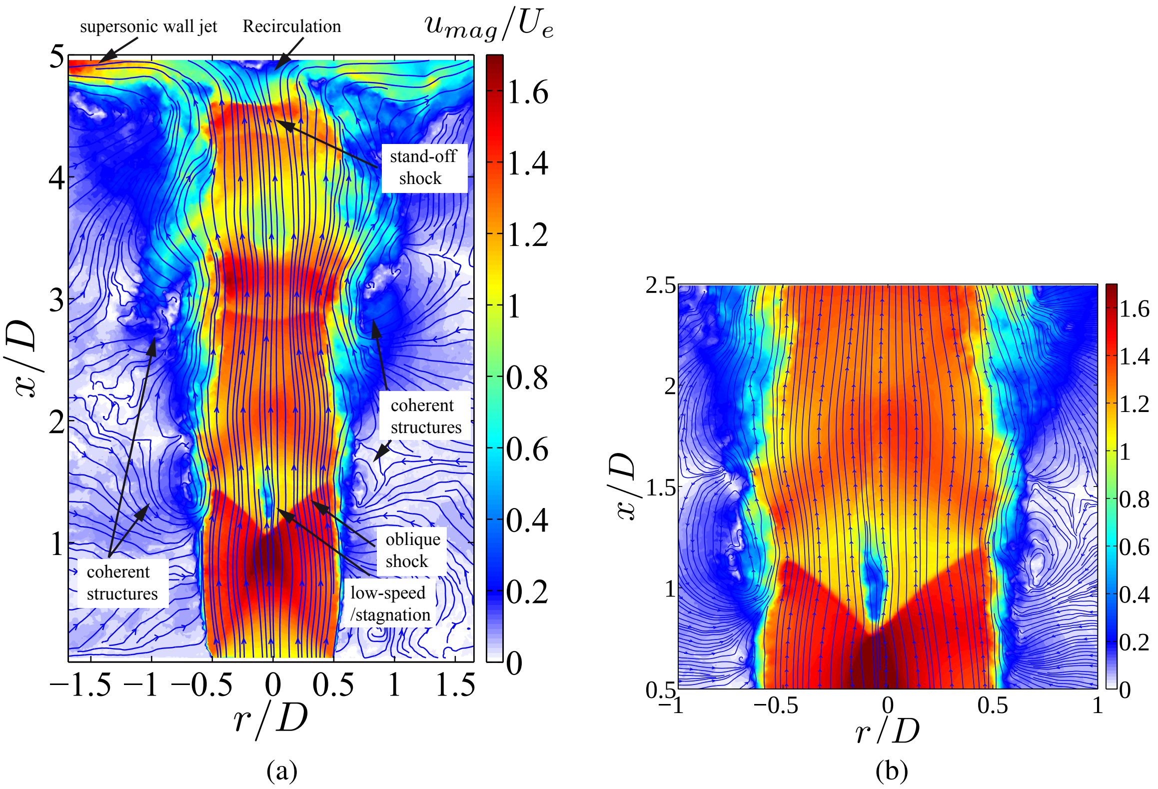

Fig. 3 Instantaneous velocity field for (a) the entire field of view (camera 1) (b) zoomed-in area (camera 2).

full domain measurement confirms the existence of these regions. At this stage, the authors believe that this phenomenon is related to the formation and disruption of the Mach disk at this specific operating and boundary condition. A stagnation bubble forms, speeds up, convects downstream, and interacts with the following shock cell. A sequence of this plausible scenario is shown in Figures 4. Velocity in this region at an early stage as shown in Figure 4(a) is very close to zero. As the region speeds up, it grows in size, and moves towards the second shock cell. Similar regions are noticed after the second shock, but they are not as strong as shown in Figure 4. It is worth noting that the measurements are not phased-locked, and therefore this sequence does not belong to a single low-speed event. This phenomenon was not noticed when the plate was removed which indicates the link between the occurrence of this event and the impingement surface. Along with this, [3] employed a triple decomposition in combination with proper orthogonal decomposition and showed that there is no recirculation zone in the Mach disk for a free jet. Further investigation is required to understand the mechanism behind the formation of the stagnation region and to investigate whether or not this phenomenon plays an important role in the feedback loop mechanism and in the flow structure.

Figure 5 shows the mean and fluctuating components of the axial and radial velocities at the centre plane of the jet. Flow statistics are symmetric along the jet centreline due to the fact that the experiment was performed with extreme caution and a large number of samples was collected. It is worth noting that the sample size is large enough so that the convergence of the first to fourth-order statistics was confirmed within the measurement uncertainty.

A periodic shock cell structure is evident from the variation of both the mean axial (Figure 5a) and radial velocity contour plots (Figure 5c). Figure 6 shows the mean and the fluctuation of the axial velocity along the jet centerline, near the shear layer, and outside the potential core. The spacing between the peaks or valleys in the mean profile represents the shock cell spacing. The oscillation of the u_{rms} along the centerline also reflects the position of the shock cells. Outside the core of the jet, the r.m.s. profile has an approximately monotonic growth towards the impingement plate, but decays as the impinging plate is approached. Along the shear layer, no monotonic growth is observed, however the oscillations that are related to the reflection points of the shock waves at the shear layer are observed.

In Figure 5(b), regions with high-level of turbulence are noticed near the shear layer and at the location of the shock cells indicative of a highly resonant and unsteady phenomenon being present there. It is worth noting that the oscillating motion of the shock cell specifically along the jet axis increases the fluctuations of the streamwise velocity component. That is more evident for shocks closer to the impingement surface. As shown previously, transverse motions of the shock waves may introduce axial oscillations [4]. Note that the artificial fluctuations imposed by the measurement also contribute to this, see [14] for further details. Figure 5(e) shows the mean azimuthal component of the vorticity normalised by the nozzle exit diameter and the jet exit velocity. The maxima of the mean out-of-plane vorticity occurs at the shear layer near the jet exit with similar levels at two sides of the jet. As is clearly observable from the contour plots, the vorticity sign changes when the jet hits the wall.

4 Concluding Remarks

An ultra high spatial resolution measurement of an impinging supersonic jet at a nozzle pressure ratio of 3.4 and a stand-off distance of 5 was performed. The complex flow structure that is a resultant of interaction of the jet with the impingement surface and acoustic field was investigated. Fine scale flow features that are well resolved including the formation of a low-speed region downstream of the first shock cell. It is found that here a stagnation bubble forms, which subsequently speeds up, convects downstream and interacts with the following shock cell. This event is possibly linked to the formation and break up of the Mach disk at this operating condition.

Acknowledgments

The financial support to conduct this research by the Australian Research Council is gratefully acknowledged. This research was undertaken with the assistance of resources provided by the National Computational Infrastructure (NCI), which is supported by the Australian Government.

References

[1] H. Assadi, F. Gaertner, T. Stoltenhoff, and H. Kreye. Bonding mechanism in cold gas spraying. *Acta Materialia*, 51(15):4379–4394, 2003.

[2] N. A. Buchmann, D. Mitchell, K. M. Ingvorsen, D. Honnery, and J. Soria. High spatial resolution imaging of a supersonic underexpanded jet impinging on a flat plate. In *Sixth Australian Conference on Laser Diagnostics in Fluid Mechanics and Combustion, Canberra, Australia, 5-7 December, 2011*, 2011.

[3] D. Edgington-Mitchell, D.R. Honnery, and J. Soria. The underexpanded jet mach disk and its associated shear layer. *Physics of Fluids*, 26(9), 2014.

[4] D. Edgington-Mitchell, K. Oberleithner, D. Honnery, and J. Soria. Coherent structure and sound production in the helical mode of a screeching axisymmetric jet. *Journal of Fluid Mechanic*, 748:822–847, 2014.

[5] K von Ellenrieder, J Kostas, and J Soria. Measurements of a wall-bounded turbulent, separated flow using HPIV. *Journal of Turbulence*, 2:1–15, 2001.

[6] M. Fedrizzi and J. Soria. Application of a single-board computer as a low cost pulse generator. *Meas Sci Tech*, under review, 2015.

[7] A Fouras and J Soria. Accuracy of out-of-plane vorticity measurements using in-plane velocity vector field data. *Experiments in Fluids*, 25:409–430, 1998.

[8] D.L. Gilmore, R.C. Dykhuizen, R.A. Neiser, T.J. Roemer, and M.F. Smith. Particle velocity and deposition efficiency in the cold spray process. *Journal of Thermal Spray Technology*, 8(4):576–582, 1999.

[9] D P Hart. PIV error correction. *Experiments in Fluids*, 29(1):13–22, 2000.

[10] B. Henderson. The connection between sound production and jet structure of the supersonic impinging jet. *Journal of the Acoustical Society of America*, 111(2):735–747, 2002.

[11] R. Kumar, A. Wiley, L. Venkatakrishnan, and F. Alvi. Role of coherent structures in supersonic impinging jets. *Physics of Fluids*, 25(7), 2013.

[12] D. Mitchell, D. Honnery, and J. Soria. Particle relaxation and its influence on the particle image velocimetry cross-correlation function. *Experiments in Fluids*, 51(4):933–947, 2011.

[13] D.M. Mitchell, D.R. Honnery, and J. Soria. The visualization of the acoustic feedback loop in impinging underexpanded supersonic jet flows using ultra-high frame rate schlieren. *Journal of Visualization*, 15(4):333–341, 2012.

[14] D.M. Mitchell, D.R. Honnery, and J. Soria. Near-field structure of underexpanded elliptic jets. *Experiments in Fluids*, 54(7), 2013.

[15] A. Powell. On edge tones and associated phenomena. *Acoustica*, 3:233–243, 1953.

[16] M Raffel, C Willert, and J Kompenhans. *Particle Image Velocimetry*. Springer, 1998.

[17] M. Raffel, C.E. Willert, S.T. Wereley, and J. Kompenhans. *Particle Image Velocimetry, A Practical Guide*. Springer, 2nd ed. edition, 2007.

[18] F. Scarano. *Particle Image Velocimetry*, volume 112 of *Springer*, chapter Overview of PIV in Supersonic Flows, pages 445–463. 2008.

[19] J. Soria. Digital cross-correlation particle image velocimetry measurements in the near wake of a circular cylinder. In *Int. Colloquium on* Jets, Wakes and Shear Layers, pages 25.1 – 25.8, Melbourne, Australia, 1994. CSIRO.

[20] J. Soria. An adaptive cross-correlation digital PIV technique for unsteady flow investigations. In A.R. Masri and D.R. Honnery, editors, *1st Australian Conference on Laser Diagnostics in Fluid Mechanics and Combustion*, pages 29–45, University of Sydney, NSW, Australia, 1996.

[21] J Soria. An investigation of the near wake of a circular cylinder using a video-based digital cross-correlation particle image velocimetry technique. *Experimental Thermal and Fluid Science*, 12:221–233, 1996.

[22] J. Soria. Multigrid approach to cross-correlation digital PIV and HPIV analysis. In *13th Australasian Fluid Mechanics Conference*, pages 381–384, Monash University, Melbourne, 1998.

[23] J Soria. Particle image velocimetry—application to turbulence studies. In *Turbulence and coherent structures in fluids, plasmas and nonlinear media*, pages 309–347. World Sci. Publ., Hackensack, NJ, 2006.

[24] J Soria, J Cater, and J Kostas. High resolution multigrid cross-correlation digital PIV measurements of a turbulent starting jet using half frame image shift film recording. *Optics & Laser Technology*, 31:3–12, July 1999.

[25] J Westerweel, D Dabiri, and M Gharib. The effect of a discrete window offset on the accuracy of cross-correlation analysis of digital PIV recordings. *Experiments in Fluids*, 23(1):20–28, 1997.

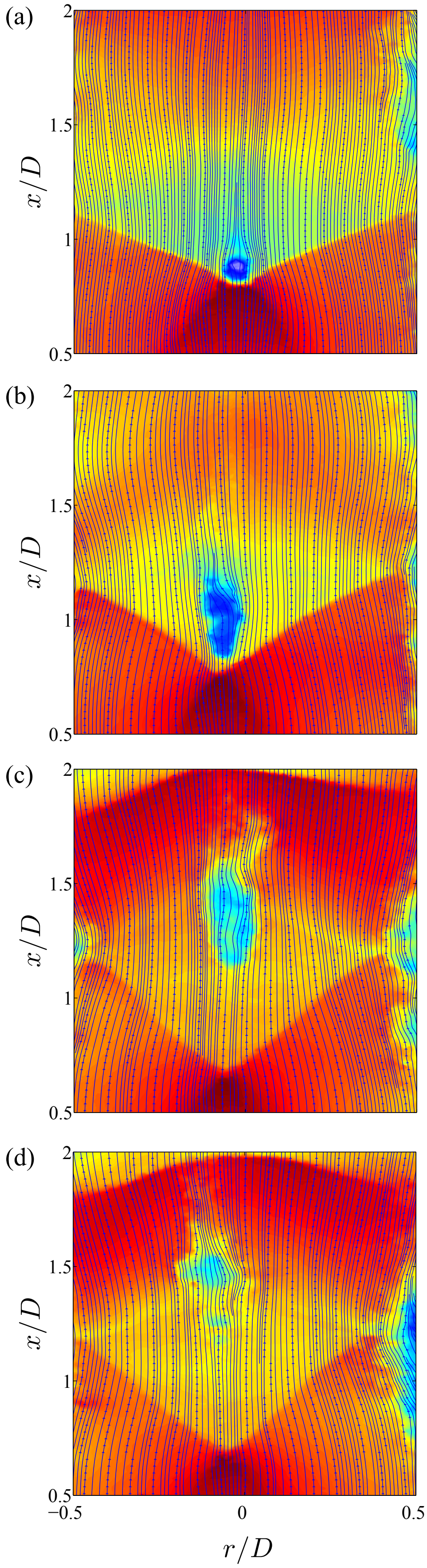

Fig. 4 A plausible trend (from a to d) for the formation and development of a subsonic region located between the first and the second shock cells. For the colour coding, see Figure 3.

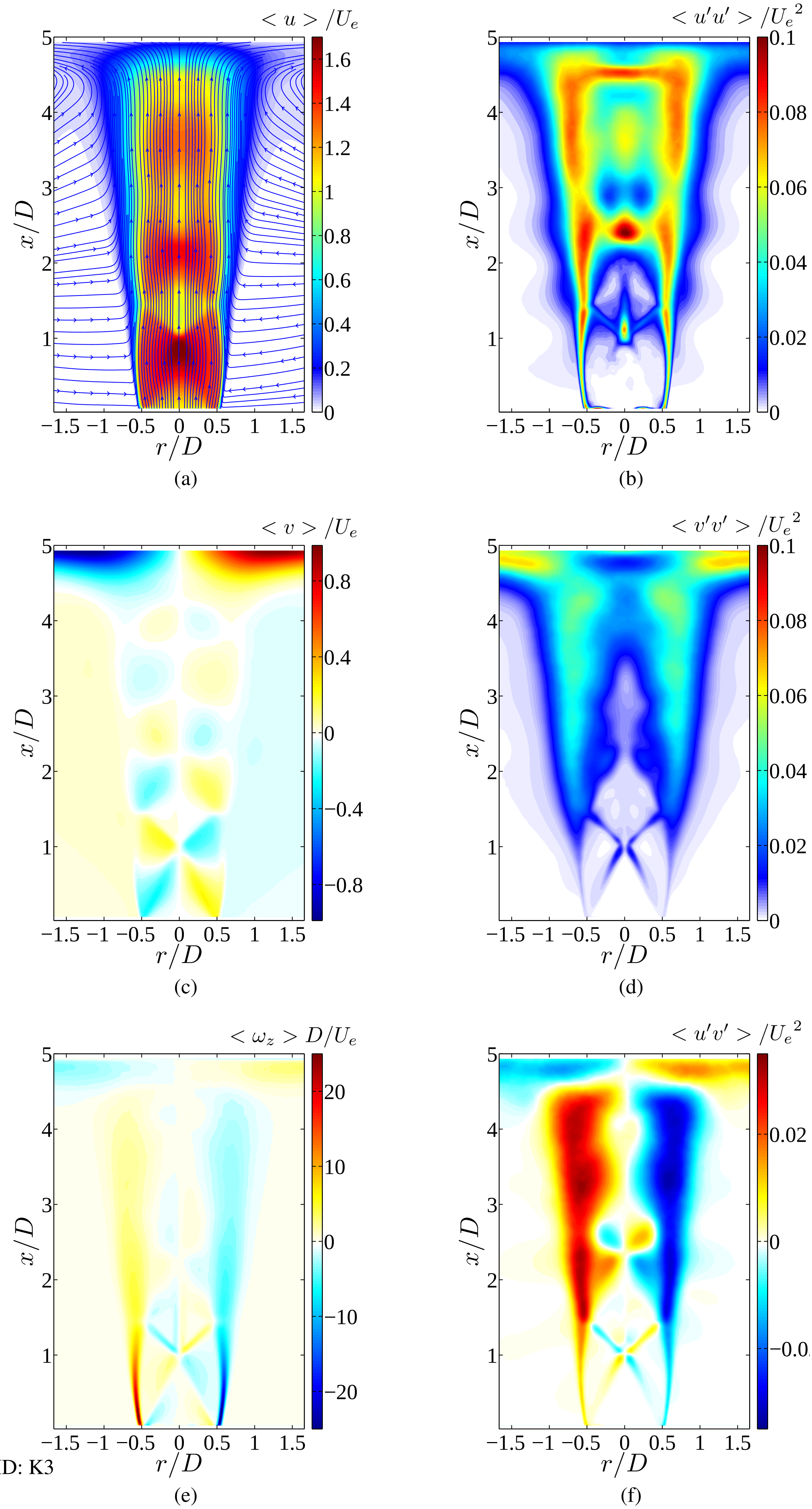

Fig. 5 First- and second-order statistics.

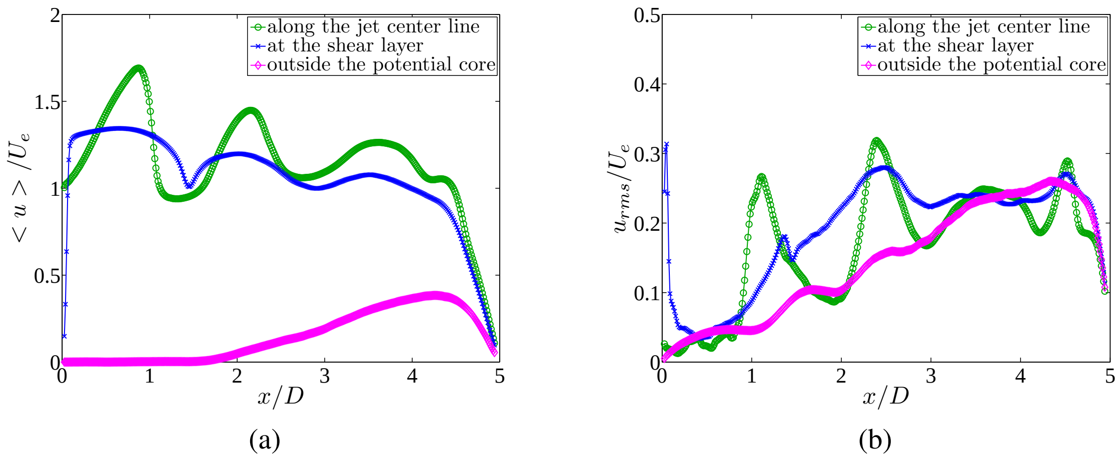

Fig. 6 (a) Mean and (b) r.m.s. of the axial velocity along the centerline of the jet, at the shear layer, and outside the potential core of the jet.